ACS APPLIED MATERIALS & INTERFACES

Research Article

www.acsami.org

Optoelectronic and Ferroelectric Properties of Cerium-Doped $(Na_{0.5}Bi_{0.5})(Ti_{0.99}Fe_{0.01})O_3$ Nanocrystalline Films on (111) $Pt/TiO_2/SiO_2/Si$: A Composition-Dependent Study

Si Zhang, Meijie Han, Jinzhong Zhang, Yawei Li, Zhigao Hu,* and Junhao Chu

Key Laboratory of Polar Materials and Devices, Ministry of Education, Department of Electronic Engineering, East China Normal University, Shanghai 200241, China

ABSTRACT: The optical and ferroelectric properties of $(Na_{0.5}Bi_{0.5})_{1-x}Ce_x(Ti_{0.99}Fe_{0.01})O_3$ (NBCTFx; $0 \le x \le 0.10$) nanocrystalline films deposited on platinized silicon ($Pt/TiO_2/SiO_2/Si$) substrates using a sol–gel method were investigated. The microstructure, surface, and cross-sectional morphology and compositions of the films were analyzed by X-ray diffraction, scanning electron microscopy, and X-ray photoelectron spectroscopy, respectively. The X-ray diffraction patterns indicate that all films are polycrystalline and show the single perovskite structure. The dielectric functions of the NBCTFx films can be uniquely extracted by fitting the measured ellipsometric spectra with a four-phase-layered model (air/surface rough layer/NBCTFx/Pt) in the photon energy range of 0.6–6.4 eV. The Tauc–Lorentz model was successfully applied and reasonably describes the spectral response behavior of ferroelectric NBCTFx films in the light-frequency region. It was found that the optical band gap and grain size decrease with increasing cerium composition because of the introduction of disorder and defects. The electrical results show that the leakage current density of the films was decreased with increasing cerium composition by reducing the density of oxygen vacancies and forming the defect complexes. The optimal ferroelectric properties were obtained in the film doped with $x = 0.10$, whose remnant polarization and coercive field values are 14.9 $\mu C/cm^2$ and 217.3 kV/cm, respectively. The present results could be crucial for future applications of lead-free ferroelectric and optoelectronic devices.

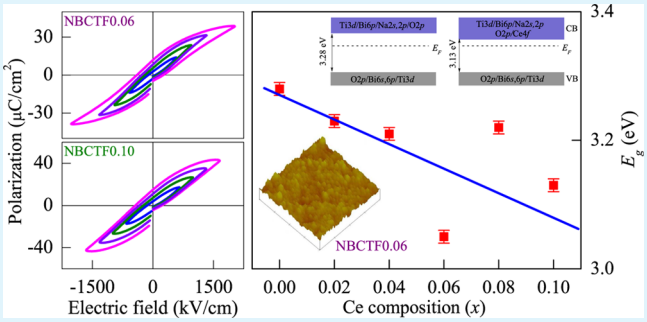

KEYWORDS: *cerium-doped $(Na_{0.5}Bi_{0.5})(Ti_{0.99}Fe_{0.01})O_3$, optoelectronic, ferroelectric, composition dependence*

1. INTRODUCTION

$Pb(Zr,Ti)O_3$ (PZT), $PbTiO_3$, $Pb(Mg,Nb)O_3$, and lead-based compounds constitute the best family of piezoelectric and ferroelectric materials that are suitable for integration in devices, such as piezoelectric actuators, sensors, and transducers.[1−3] However, these materials contain too much toxic lead, which leads to severe environmental and health problems. Therefore, studies on lead-free materials have attracted much attention recently. Sodium bismuth titanate $Na_{0.5}Bi_{0.5}TiO_3$ (NBT), a ferroelectric complex perovskite-structure compound with two different ions at the A site of the ABO_3 structure,[4] was considered to be one of the promising candidates for lead-free ferroelectric and piezoelectric devices.[5−7] Pure NBT is a ferroelectric material, which has a relatively high Curie temperature of T_c = 320 °C, a relatively large remanent polarization of P_r = 38 $\mu C/cm^2$, and a coercive field of E_c = 73 kV/cm at room temperature.[8] However, undoped NBT exhibits low piezoelectric coefficients and electric-field-induced strain.[9] In order to improve this system and make it a more available substitute, chemical substitution/doping can be used to modify the piezoelectric and ferroelectric properties.[10] It was found that iron substitution leads to an enhanced piezoelectric coefficient,[11] and the addition of cerium plays an important role in improving the ferroelectric properties of NBT crystals by increasing the remnant polarization and coercive field.[12] Another reason for choosing the Ce ion is for its interesting performance in ceramics and its closer ionic radius to A site ions.[12] Moreover, the sodium-containing compounds were exclusively investigated as bulk crystals and ceramics until now,[13−15] and only a few studies were done for films in spite of the fact that they offer excellent ferroelectric and optical properties.[16−18] Recently, a reduced leakage current and enhanced ferroelectric properties can be obtained in a (Ce,Fe)-codoped NBT film.[19] Thus, it is necessary to further study the fabrication and optoelectronic and electrical properties of $(Na_{0.5}Bi_{0.5})_{1-x}Ce_x(Ti_{0.99}Fe_{0.01})O_3$ (NBCTFx) films in order to develop some promising devices.

On the other hand, Bujakiewicz-Koroska and Natanzon used a generalized gradient approximation method to obtain a band gap of about 2 eV for NBT.[20] The prediction of the band gap indicates that NBT is a good optical material. Moreover, it was found that a NBT single crystal presents good piezoelectric

Received: January 16, 2013
Accepted: April 1, 2013
Published: April 1, 2013

   dx.doi.org/10.1021/am400196c | ACS Appl. Mater. Interfaces 2013, 5, 3191−3198

properties and rich optical properties,[21−24] which shows that it could be important for future applications of optoelectronic devices. As is known, the electronic structure of the material decides whether it is proper for the applications of optical and electric devices. However, few studies on the optical properties have been carried out, and the investigation of its electronic structure is seriously limited for the NBT system, especially for the (Ce,Fe)-codoped NBT material. Spectroscopic ellipsometry (SE) is considered to be a spectral technique to extract dielectric functions of films. SE based on the reflectance configuration is easily adopted for the determination of optical constants.[25] It is a powerful and nondestructive tool that is sensitive to ultrathin films and surfaces and allows us to obtain the thickness and optical characteristics of a multilayer system without the Kramers−Krönig transformation (KKT) due to the determination of two independent physical parameters simultaneously.[26] Therefore, this makes it possible to investigate the optical properties of NBCTF*x* films in a wider photon energy range. In order to explain the distinguishing physical phenomena and further exploit the cerium-substituted NBTF material as an available candidate for fabricating piezoelectric actuators and sensors, the cerium-related optical properties and/or electronic structures should be thoroughly studied, which can provide a critical reference to the device designs and performance optimizations.

In this article, NBCTF*x* ($0 \le x \le 0.10$) films were prepared by the sol−gel method. The microstructure, surface morphology, electronic structure, and ferroelectric properties of the NBCTF*x* films with different cerium compositions were investigated. It was found that cerium doping induced variation of the film microstructure. The dielectric functions from the near-infrared (NIR) to ultraviolet (UV) photon energy range were extracted by the SE technique. The effects of the cerium composition on the optical and electrical properties of NBCTF*x* films are discussed in detail.

2. EXPERIMENTAL DETAILS

Fabrication of NBCTF*x* ($0 \le x \le 0.10$) Films. Analytically pure bismuth nitrate [$Bi(NO_3)_3{\cdot}5H_2O$, 99.0%], sodium acetate trihydrate ($CH_3COONa{\cdot}3H_2O$, 99.0%), titanium butoxide ($Ti[O(CH_2)_3CH_3]_4$, 98.0%), ferric nitrate ninehydrate [$Fe(NO_3)_3{\cdot}9H_2O$, 98.5%], and cerium nitrate hexahydrate [$Ce(NO_3)_3{\cdot}6H_2O$, 99.9%] were used as the starting materials. As shown in Scheme 1, the required $Bi(NO_3)_3{\cdot}5H_2O$ and $CH_3COONa{\cdot}3H_2O$ were mixed in the required molar ratio of bismuth and sodium and then dissolved in a mixture of ethylene glycol ($C_2H_6O_2$, 99.0%) and acetic acid (CH_3COOH, 99.5%) with a volume ratio of 1:2. After the solution was stable and became transparent and homogeneous by magnetic stirring, the required $Fe(NO_3)_3{\cdot}9H_2O$ and $Ce(NO_3)_3{\cdot}6H_2O$ were added into the solution. Stirring was continuous until they were completely dissolved. A significant loss of bismuth can be expected because of evaporation in the form of bismuth oxide (Bi_2O_3) during thermal annealing. However, heat treatments at high temperatures are normally necessary to obtain well-crystallized films by chemical solution deposition. Long heat treatments can cause much damage, such as stacking, interdiffusion between the film and substrate, and loss of stoichiometry. Therefore, excess bismuth of about 5 mol % was used to compensate for bismuth loss during the annealing process.[27] An appropriate amount of acetylacetone ($C_5H_8O_2$, 99.0%) was added to stabilize the solution. Finally, the proper amount of $Ti[O(CH_2)_3CH_3]_4$ was also added into the solution. The mixture was stirred constantly until a transparent and stable precursor solution was obtained. The solutions of NBTF and NBCTF0.10 can be obtained by the method mentioned above, and the rest of the solutions were obtained by mixing the two solutions with different volume ratios. Magnetic stirring was carried out again for 1 day, the solutions of the NBCTF*x* were 0.3 M, and they were obtained as precursors for film deposition.

Scheme 1. Preparation Process of the Precursor and Film for NBCTF0.10

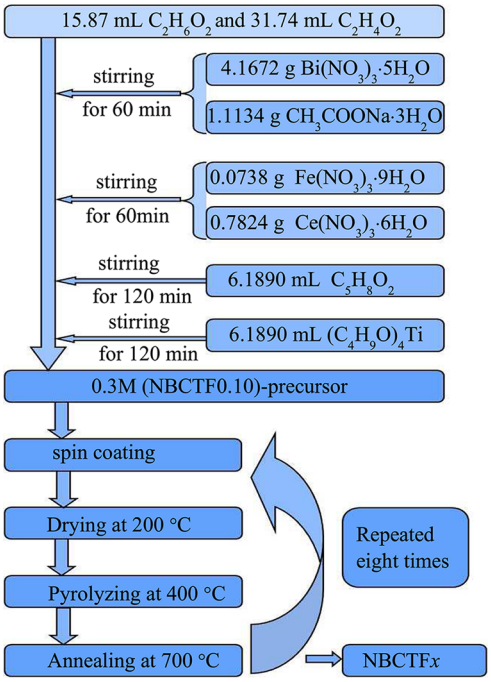

As is known, the $Pt/TiO_2/SiO_2/Si$ substrates can improve the electrical properties of perovskite-type ferroelectric films because of the well-defined lattice match. Moreover, the platinum layer can be taken as the bottom electrode for the electrical experiments. Before deposition of the NBCTF*x* nanocrystalline films, the $Pt/TiO_2/SiO_2/Si$ substrates were cleaned in pure ethanol to remove physisorbed organic molecules from the surfaces and then the substrates were rinsed repeatedly with deionized water. The films were deposited by spin coating onto the $(111)Pt/TiO_2/SiO_2/Si$ substrates at a speed of 4000 rpm for 20 s. Each layer of the films was dried at 200 °C for 200 s and then pyrolyzed at 400 °C for 240 s to remove residual organic compounds, followed by annealing at 700 °C for 300 s in ambient air by a rapid thermal annealing procedure. The spin-coating and annealing-treatment procedures were repeated eight times to obtain the desired thickness.

XRD, AFM, SEM, XPS, SE, and Ferroelectric Measurements. The crystalline structures of the NBCTF*x* nanocrystalline films were analyzed by X-ray diffraction (XRD) using Ni-filtered Cu Kα radiation (Bruker D8 Advance diffractometer, Germany) under an accelerating voltage of 40 kV and a scanning rate of 3° at 2θ/min. The surface morphology of the films was examined by atomic force microscopy (AFM; Digital Instruments Dimension 3100, Veeco). The scale height was 20 nm, and the measured area was 2×2 μm^2. The surface morphology and thickness of the films were examined by field-emission scanning electron microscopy (FESEM; Philips XL30FEG). X-ray photoelectron spectroscopy (XPS) experiments were carried out on a RBD upgraded PHI-5000C ESCA system (Perkin-Elmer) with Mg Kα radiation ($h\nu$ = 1253.6 eV). The ellipsometric measurements were carried out by a NIR−UV SE in the wavelength range of 195−2000 nm (0.6−6.4 eV) with a spectral resolution of 2 nm (V-VASE by J. A. Woollam Co., Inc.). The incident angle was selected as 70° for the films corresponding to the experimental optimization near the Brewster angle. The hysteresis loops of the NBCTF*x* films were measured by a ferroelectric test system (Percision LC, Radiant Technologies, Inc.). The leakage current−voltage (I−V) characteristics were measured using an electrometer (Keithley 6517A). Note that the films were measured at room temperature, and no mathematical smoothing was performed on the experimental data.

3. RESULTS AND DISCUSSION

Structural Analysis. The XRD patterns of the NBCTF*x* films with different cerium compositions annealed at 700 °C are shown in Figure 1a. It can be seen that all of the films are

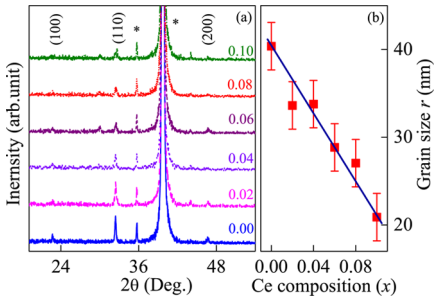

Figure 1. (a) XRD patterns of the NBTF, NBCTF0.02, NBCTF0.04, NBCTF0.06, NBCTF0.08, and NBCTF0.10 films deposited on Pt/TiO_2/SiO_2/Si substrates. Note that the symbol * indicates the observed trace of the Pt/TiO_2/SiO_2/Si substrate. (b) Grain size *r* of the NBCTF*x* films as a function of the cerium composition.

polycrystalline with a stronger (110) diffraction peak, whose position (2θ) is located at about 32.4°. Besides the strong feature, there are several other weaker diffraction peaks (100) and (200), etc., and no impurity phase is observed, which confirms that the films are of a single perovskite phase. As the cerium composition increases, these diffraction peaks become weaker and broadening. This suggests that the Ce atoms were successfully incorporated into the host lattice. Furthermore, the grain size (*r*) can be calculated from the (110) diffraction peak according to the well-known Scherrer's equation. As can be found from Figure 1b, the grain size decreases with increasing cerium composition and the grain size (about 20.9 nm) of the NBCTF0.10 film is the smallest because of the largest value of the full width at half-maximum (fwhm). Figure 2 shows the three-dimensional AFM images of the NBCTF*x* films. This suggests that the surface morphology presents a similar pattern, while the root-mean-square roughness values are estimated to

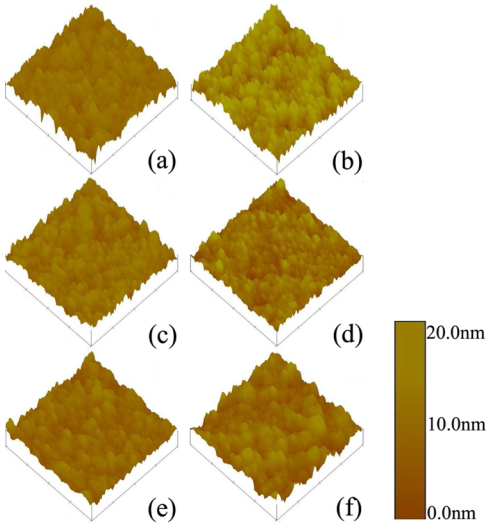

Figure 2. Three-dimensional AFM images of (a) NBTF, (b) NBCTF0.02, (c) NBCTF0.04, (d) NBCTF0.06, (e) NBCTF0.08, and (f) NBCTF0.10, respectively. Note that the scale height is 20 nm, and the measured area is 2 × 2 μm^2.

3.7, 4.1, 3.0, 2.4, 2.8, and 3.7 nm for *x* = 0.00, 0.02, 0.04, 0.06, 0.08, and 0.10, respectively. The surface and cross-sectional SEM images of the NBTF, NBCTF0.02, NBCTF0.04, NBCTF0.06, NBCTFC0.08, and NBCTF0.10 films are shown in Figure 3. There is an obvious interface between the film and platinum substrate, which indicates that the films are crack-free and uniform. Besides, with increasing cerium composition, the films become denser, which indicates that less voids appear on the surface. It can be concluded from the cross-sectional pictures that the films are compacted and the thicknesses of the NBCTF*x* films are 167, 179, 193, 202, 207, and 211 nm for *x* = 0.00, 0.02, 0.04, 0.06, 0.08, and 0.10, respectively, which indicated that the thicknesses of the films slightly increase with increasing cerium composition. Owing to identical growth conditions, the NBCTF*x* films present similar morphology with cerium replacement, indicating that the films are highly homogeneous. On the basis of the XRD patterns and SEM images, it is confirmed that all films are well-crystallized and crack-free. Nevertheless, the remarkable variation on the crystalline structure can obviously affect the dielectric constants, optical band gaps, and electrical properties discussed in the following.

XPS of the NBCTF*x* (0 ≤ *x* ≤ 0.10) Films. Elemental compositions and chemical states of the NBCTF*x* nanocrystalline films were studied by XPS measurements. The survey spectra for all films indicate that only C 1s, Na 1s, Bi 4f, Ti 2p, O 1s, Fe 2p, and Ce 3d related core levels can be detectable. The C 1s peak at 284.6 eV is used as an internal standard, and the other spectra are calibrated with the C 1s peak to correct the binding energy position. In order to obtain separate information, the XPS data were fitted by Lorentzian−Gaussian functions, which depends on the following parameters: peak position, fwhm, and peak area. The fitting quality can be found in Figure 4. As an example, high-resolution spectra of Ti 2p, Bi 4f, Ce 3d, and O 1s for the NBCTF0.10 film are presented in Figure 4. The Ti 2p XPS spectra of NBCTF0.10 were observed at 458 and 464.4 eV for the $2p_{3/2}$ and $2p_{1/2}$ peaks, respectively, as shown in Figure 4a. The Bi 4f XPS spectra of NBCTF0.10 were observed at 158.5 and 163.8 eV for the $4f_{7/2}$ and $4f_{5/2}$ peaks in Figure 4b. The XPS data suggest that the Ti ion is of the 4+ valence state and the Bi ion is of the 3+ valence state. The Fe 2p XPS spectrum of NBCTF0.10 was observed at 711.9 eV for the $2p_{3/2}$ peak, which indicates that the Fe ion is of the 2+ valence state. The Na 1s XPS spectrum of NBCTF0.10 was observed at 1071 eV for the 1s peak. It should be noted that the Ce 3d XPS spectra of NBCTF0.10 were observed at 899 and 917 eV for the $3d_{5/2}$ and $3d_{3/2}$ peaks in Figure 4c. The peak corresponding to the 917 eV binding energy is clearly visible and based on the previous studies in the literature,[28−30] this unquestionably proves the IV oxidation state for cerium, which is in good agreement with the findings in the core level spectra of the CeO_2 film.[31] Therefore, the XPS data suggest that the Ce ion is of the 4+ electronic state.

In addition, deconvolution of the O 1s XPS spectra for the NBCTF0.10 film is fitted by two components, as can be seen in Figure 4d. As an example, one of the O 1s peaks of NBCTF0.10 located at 529.0 eV is ascribed to the lattice oxygen of the NBCTF0.10 film, while the higher binding energy peak at about 530.2 eV in O 1s for the NBCTF0.10 film reveals the presence of the chemisorbed oxygen-containing species. The relatively high intensity of the "O_{chem}" component is due to the good surface sensitivity.[32] Table 1 shows the atomic concentrations of the NBCTF*x* films from fitting of the XPS

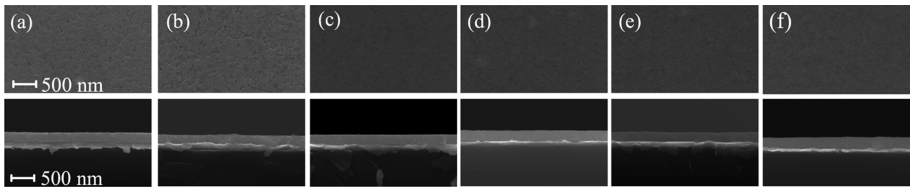

Figure 3. Surface and cross-sectional SEM images of (a) NBTF, (b) NBCTF0.02, (c) NBCTF0.04, (d) NBCTF0.06, (e) NBCTF0.08, and (f) NBCTF0.10 films, respectively. Note that the scale bars for all of the images are 500 nm.

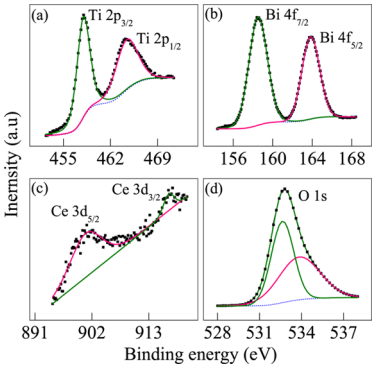

Figure 4. XPS spectra of the (a) Ti 2p, (b) Bi 4f, (c) Ce 3d, and (d) O 1s regions for the NBCTF0.10 film. Note that the dotted and solid lines indicate the experimental data and fitting results, respectively.

Table 1. Atomic Concentrations of the NBCTF*x* Films As Determined from XPS Measurements

	XPS atomic concentration (atom %)					
sample	Na	Bi	Ti	O	Ce	Fe
x = 0.00	4.0	8.0	22.3	64.7		0.54
x =0.02	3.9	8.3	22.2	64.5	0.7	0.46
x = 0.04	3.3	8.1	21.8	64.9	1.8	0.53
x = 0.06	3.5	7.2	19.3	67.1	2.6	0.38
x = 0.08	3.0	7.2	19.2	67.3	2.7	0.62
x = 0.10	5.3	6.6	21.0	63.6	2.9	0.62

peak areas with the sensitivity factors. It can be seen that the concentration of cerium increases readily with increasing doping. The atomic concentration of bismuth is larger than that of sodium, which is due to the fact that excess bismuth is added to compensate for the bismuth loss during the annealing process. As discussed previously, this indicates that the oxidation state of cerium is 4+ from the XPS data. In the perovskite cell, the ion at the A site $[(Na_{0.5}Bi_{0.5})]$ has a coordination number of 12. The size of the 12-coordinated $(Na_{0.5}Bi_{0.5})^{2+}$ ion is 135 pm, while the 12-coordinated Ce^{4+} has an ionic radius of 114 pm, which indicates that the size difference is only 15.6%.[33] On the other hand, the ion at the B site (Ti site) in the perovskite cell has a coordination number of 6 and the size of the 6-coordinated Ti^{4+} ion is 60.5 pm. The 6-coordinated Ce^{4+} has an ionic radius of 87 pm, and the size difference is evaluated to 31%.[33] Therefore, it can be more likely to substitute for $(Na_{0.5}Bi_{0.5})^{2+}$ as a donor dopant when Ce^{4+} is doped into the perovskite-type NBT.

Electronic Band Structure. In order to extract the dielectric functions $[\tilde{\varepsilon}(E) = \varepsilon_r(E) + i\varepsilon_i(E)]$ and other physical parameters of the ferroelectric NBCTF*x* nanocrystalline films on the (111) $Pt/TiO_2/SiO_2/Si$ substrates, the SE spectra were studied by a multilayer model with the four-phase-layered structure (air/surface rough layer (SRL)/NBCTF*x*/Pt). It should be emphasized that the reliability of the fitting method mainly depends on the selection of the dielectric function models. The dielectric response of the semiconductor/dielectric materials in the light-frequency region can result from the interband electronic transitions. A dielectric function derived from the direct band-gap theory is desirable for the NBCTF*x* films. There are many dispersion functions expressing the interband transition contributions. Fortunately, the Tauc–Lorentz (TL) model is one of the useful functions to express the dielectric dispersion of the perovskite systems in the light-frequency region. Therefore, the TL model was applied to express the optical dispersion of the NBCTF*x* films studied.[34,35] The TL dielectric function standard quantum-mechanical or Lorentz calculation for ε_2 (the imaginary part of the complex dielectric function) of a collection of noninteracting atoms was widely applied in many solid materials from the transparent to strong absorption region.[36] The imaginary part can be written as

$$\varepsilon_2(E) = \begin{cases} \dfrac{A_0 E_n C (E - E_g)^2}{(E^2 - E_n{}^2)^2 + C^2 E^2} \dfrac{1}{E} & (E > E_g) \\ 0 & (E \le E_g) \end{cases} \quad (1)$$

and the real part is given by the KKT

$$\varepsilon_1(E) = \varepsilon_\infty + \frac{2}{\pi} P \int_{E_g}^{\infty} \frac{\xi \varepsilon_2(\xi)}{\xi^2 - E^2} \, d\xi \quad (2)$$

Equations 1 and 2 depend on the following five parameters: the transition matrix element A_0, the peak transition energy E_n, the broadening term C, the band-gap energy E_g, and the high-frequency dielectric constant ε_∞. In order to exclude surface fluctuation effects from the high-temperature annealing, a SRL must be taken into account.[37,38] Therefore, a four-layered model (air/SRL/NBCTF*x*/Pt) was found to reproduce the ellipsometric spectra quite well. The dielectric function of the SRL as a mixture of 50% NBCTF*x* and 50% voids was expressed with the aid of a Brüggeman effective medium approximation.[39]

As an example, the experimental spectra Ψ and Δ of the NBCTF*x* films with cerium compositions of 0.00, 0.04, and 0.10 are shown by the dotted lines in parts a and b of Figure 5, respectively. The Fabry-Pérot interference patterns due to the thicknesses of the NBCTF*x* films are observed below the photon energy of 3.8 eV, indicating that the films are transparent in the photon energy region. The dielectric function of the NBCTF*x* films can be uniquely extracted by fitting the model function to the measured data. The fitted parameter values in eqs 1 and 2 and thicknesses are summarized in Table 2, and the fitted ellipsometric spectra Ψ and Δ are shown by the solid lines in parts a and b of Figure 5, respectively. As can be seen, a good agreement is obtained between the experimental and fitting spectra in the entirely

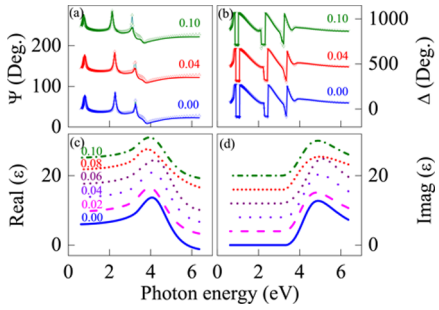

Figure 5. NIR–UV experimental (dotted lines) and best-fitted ellipsometric (solid lines) spectra (a) $\Psi(E)$ and (b) $\Delta(E)$ of the NBTF, NBCTF0.04, and NBCTF0.10 films. Evolution of (c) the real part ε_1 and (d) the imaginary part ε_2 of the NBCTFx films in the photon energy ranges from 0.6 to 6.4 eV. Note that Ψ, Δ, ε_1, and ε_2 are vertically shifted by adding 100, 400, 4, and 4, respectively.

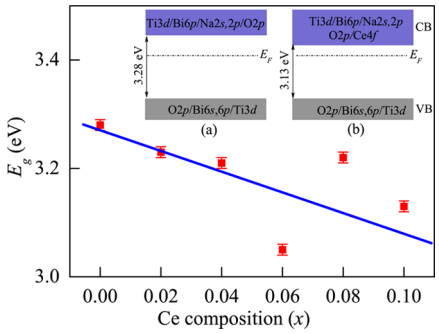

Figure 6. Linear fitting result of E_g as a function of the cerium composition for the NBCTFx films. The inset shows the schematic representation of the electronic band structure for (a) NBTF and (b) NBCTF0.10 films, where E_F denotes the Fermi energy level.

measured photon energy range. The evaluated dielectric function of the NBCTFx film is shown in Figure 5c,d. The evolution of ε with the photon energy is a typical optical response behavior of semiconductor materials. As can be seen in Figure 5d, ε_2 increases with the photon energy and approaches the maximum at around 4.5 eV, which indicates that a strong optical absorption appears. However, the parameter ε_1 increases with the photon energy and approaches the maximum value at around 4.0 eV, which indicates a transition and ascent of the absorption edge, and then the dielectric function decreases toward the higher energy because of the known Van Hove singularities. It should be emphasized that the maximum values of the real and imaginary parts are consistent because of the KKT.

As can be seen from Figure 6, the optical band gap (E_g) of the films decreases with the cerium composition, which is slightly larger than that (3.03 eV) of an NBT single crystal.[40] The band structure calculation reveals that NBT has a direct band gap of 2.1 eV.[40] It should be emphasized that the calculated band gap is much smaller than the experimental value (3.28 eV). It is well-known that the dielectric function can be directly related to the electronic band structure of the material. Especially, the imaginary part can give electronic transition information. Therefore, the optical function can provide important insight on the dielectric and ferroelectric behavior of the NBCTFx material. Unfortunately, there have been few reports on the electronic band structure of the NBCTFx films. Compared with the result calculated by Zeng et al., the peak obtained in the experiment corresponds mainly to the transitions from the O 2p valence band (VB) to the Ti 3d or Bi 6p lower-energy conduction band (CB). The electric properties of NBCTFx as well as the optical properties are considered to be determined by the charge-transfer transitions from O 2p to Ti 3d or Bi 6p states. Furthermore, the VB mainly consists of the O 2p, Bi 6s6p, and Ti 3d states in the perovskite-type unit, and the O 2p orbital is strongly hybridized with the Ti 3d (O 2p–Ti 3d) and Bi (O 2p–Bi 6s6p) orbital below the Fermi level E_F. However, the CB is dominated by Ti 3d states and Bi 6p and Na 2s2p with minor contributions from O 2p states. Also, there is considerable hybridization between Ti 3d, Bi 6p, Na 2s2p, and O 2p in the CB.[40] In the case of cerium-substituted NBTF films, the Ce atoms substitute the partial Bi and Na atoms in the pseudoperovskite unit. E_g of the films decreases with the cerium composition because the Ce^{4+} ions show a 4+ valence state, which is higher than $(Na_{0.5}Bi_{0.5})^{2+}$. Thus, the substitution of Ce atoms can contribute extra electrons to CB, as shown in the inset of Figure 6. With increasing cerium composition, more and more electrons were produced, which pushes the CB toward E_F. Besides, the optical band gap is expected to decrease because of the increase of disorder and defects with increasing cerium concentration. Because cerium doping will introduce defects into the NBCTFx films, which act as trap sites and can, consequently, give rise to new transition states of variable energy. In other words, the optical band gap of the films decreases with the cerium composition.

Electrical Properties. Figure 7 shows the typical polarization–electric field (P–E) hysteresis loops of the nanocrystalline films. As can be seen, the data of the NBCTF0.06, NBCTF0.08, and NBCTF0.10 films were obtained after several cycles, which enabled a fully saturated response, while NBTF, NBCTF0.02, and NBCTF0.04 films cannot reach the saturated state, which indicates that they show poor ferroelectric properties, and the NBCTF0.06, NBCTF0.08, and NBCTF0.10 films exhibit optimized P–E loops. The remnant polarization (P_r) of the NBCTF0.06, NBCTF0.08, and NBCTF0.10 films are 10.2, 14, and 14.9 $\mu C/cm^2$ under an

Table 2. Parameter Values of the TL Dielectric Function Model for the NBCTFx Films Determined from the Simulation of Ellipsometric Spectra in Figure 5[a]

sample	ε_∞	A_0 (eV)	E_g (eV)	E_n (eV)	C (eV)	d_s (nm)	d_f (nm)
NBTF	1.16 ± 0.12	327 ± 9	3.28 ± 0.01	4.41 ± 0.02	2.11 ± 0.12	8.4 ± 0.3	147 ± 1
NBCTF0.02	1.13 ± 0.16	326 ± 16	3.23 ± 0.01	4.23 ± 0.02	2.24 ± 0.19	12 ± 1.0	154 ± 1
NBCTF0.04	1.00 ± 0.16	281 ± 11	3.21 ± 0.01	4.54 ± 0.04	2.29 ± 0.21	8.9 ± 2.5	153 ± 1
NBCTF0.06	1.00 ± 0.05	207 ± 6	3.05 ± 0.01	4.81 ± 0.03	2.30 ± 0.14	10.1 ± 1.6	165 ± 1
NBCTF0.08	1.00 ± 0.25	424 ± 17	3.22 ± 0.01	3.82 ± 0.02	2.87 ± 0.28	8.8 ± 0.4	162 ± 2
NBCTF0.10	1.03 ± 0.21	249 ± 17	3.13 ± 0.01	4.34 ± 0.05	2.42 ± 0.31	7.9 ± 3.2	177 ± 2

[a]The 95% reliability of the fitting parameters is given with standard deviation.

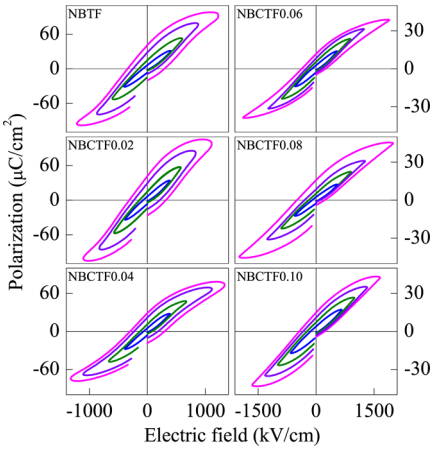

Figure 7. *P*–*E* hysteresis loops of the NBTF, NBCTF0.02, NBCTF0.04, NBCTF0.06, NBCTF0.08, and NBCTF0.10 films as a function of the electric field measured at 10 kHz and room temperature.

applied voltage of 30 V, respectively, which are larger than other NBT-based films and single crystals.[12,41] That is to say, the optimal ferroelectric properties were obtained in the film doped with $x = 0.10$.

Figure 8 shows the leakage current density versus electric field (J–E) characteristics of the NBCTFx films. The leakage

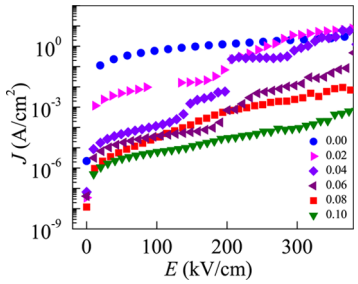

Figure 8. Leakage current density J as a function of the electric field E for the NBCTFx (x = 0.00, 0.02, 0.04, 0.06, 0.08, and 0.10) films.

current density increase sharply with the applied electric field and decrease with increasing cerium composition. Note that the leakage current density in the NBCTF0.10 film at 300 kV/cm is about 4 orders of magnitude lower than that in the NBTF film. For the case of the NBCTFx film, owing to the higher valence of Ce^{4+} than that of $(Na_{0.5}Bi_{0.5})^{2+}$ and the constraint of the electrical charge neutrality, Ce ion replacement will restrain the formation of oxygen vacancies. Fe ion substitution induces the defect complexes between the acceptors and oxygen vacancies, and the electric field required for generating the mobile oxygen vacancies will increase because it needs more electric energy to overcome the electrostatic attraction force of defect complexes.[19] As cerium doping increased, more oxygen vacancies were suppressed and more defect complexes were formed, which will also reduce the leakage current density and optimize the ferroelectricity. The vacancies created by this process can be explained by the following reaction: $CeO_2 + 2(A_{A^{2+}}^{2+})^X + V_O^{\bullet\bullet} \leftrightarrow (Ce_{A^{2+}}^{4+})^{\bullet} + (O_{O^{2-}}^{2-})^X + 2AO\uparrow$, where A represents $Na_{0.5}Bi_{0.5}$. Every Ce ion added to the structure will compensate for one oxygen vacancy. Therefore, Ce ion replacement will restrain the formation of oxygen vacancies. The electrical properties of the perovskite-type films are basically controlled by point defects in the structure. Before the discussion of the measured leakage current behavior, the possible point defects are evaluated. The sources of these defects in perovskites are bismuth volatilization and acceptor or donor doping elements. $Na_{0.5}Bi_{0.5}$ vacancies and holes are created as a result of this bismuth oxide evaporation. On the other hand, because of the oxygen loss from the structure, oxygen vacancies and more electrons are created because of reduction. These point defects can be expressed by the Kröger–Vink notation: $(A_{A^{2+}}^{2+})^X + (O_{O^{2-}}^{2-})^X \leftrightarrow AO\uparrow + V_A'' + V_O^{\bullet\bullet} + 2h^{\bullet} + 2e'$ and $^1/_2O_2 + V_O^{\bullet\bullet} \leftrightarrow (O_{O^{2-}}^{2-})^X + 2h^{\bullet}$, where A represents $Na_{0.5}Bi_{0.5}$. Cations are separated from each other with O ions in the perovskite structure. Therefore, a cation vacancy should overcome a large energy barrier to move.

On the other hand, O ions are connected with each other. Thus, oxygen vacancies can move easily with a lower energy compared with the cation vacancies.[42] For this reason, the main active and highly mobile ionic component in the perovskite-type NBCTFx films are oxygen vacancies. When these materials are annealed under oxygen-rich or regular atmospheric conditions, oxygen might be reintroduced into the structure and the concentration of oxygen vacancies decreases. It is clearly seen from Figure 8 that cerium doping causes a significant decrease in the leakage current density. This improvement is thought to be related to the 4+ valence state of cerium, which was confirmed by a detailed XPS analysis. The Ce^{4+} replaces the $(Na_{0.5}Bi_{0.5})^{2+}$ cation in the perovskite structure as a donor dopant. In the $Na_{0.5}Bi_{0.5}$ deficient compositions of the perovskite structure, cerium doping fills some of the $(Na_{0.5}Bi_{0.5})$ vacancies and leaves some unfilled. Therefore, a number of deep traps are left for holes. In the case of $Na_{0.5}Bi_{0.5}$ excess compositions, however, cerium doping decreases the number of oxygen vacancies. Because the mobility of the oxygen vacancies is one of the main mechanisms of charge transport and therefore one of the main contributors to the leakage current in the NBCTFx thin films, any dopant decreasing the concentration of oxygen vacancies will consequently cause a drop in the leakage current. Therefore, the decrease of the leakage current density due to cerium addition can be explained. On the other hand, it was reported that the leakage current density may be caused by some accidental factors, such as an uneven contact surface between the film and platinum electrodes. Note that the platinum electrodes will recrystallize into large grains after the annealing process, which will smooth the contact layer between the film and platinum electrodes and further remove the point discharge. The phenomena can be confirmed by the SEM pictures (Figure 3), suggesting that there is a distinct interface between the layer and substrate, as previously discussed.

In order to find out the leakage mechanism of the NBCTFx nanocrystalline films, several conduction mechanisms of the leakage current were provided, such as Schottky emission,[43−45] Frenkel–Poole emission,[46] Fowler–Nordheim tunneling, direct tunneling, and space-charge-limited current (SCLC).[47] The Schottky emission can be expressed as[48] $J = AT^2 \exp\{-q[\varphi_B - (qE/4\pi\varepsilon_0\varepsilon_r)^{1/2}]/kT\}$, where A, $q\phi_B$, ε_0, and ε_r are the effective Richardson constant, potential barrier height, permittivity of free space, and dynamic dielectric constant, respectively. The Schottky emission mechanism is an electrode-limited conduction, where the entire leakage current is dominated by the Schottky barrier generated at the interface of the electrode and films. If the conduction current is governed by the Schottky emission, the $\log(J)$ versus $E^{1/2}$ (where J and E are the leakage

current density and applied electrical field, respectively) plot should be a straight line and the slope will give the dynamic dielectric constant. As an example, the Schottky emission plots with the dynamic dielectric constant fitted for the NBCTF0.08 and NBCTF0.10 films are shown in Figure 9a,c, where linearity

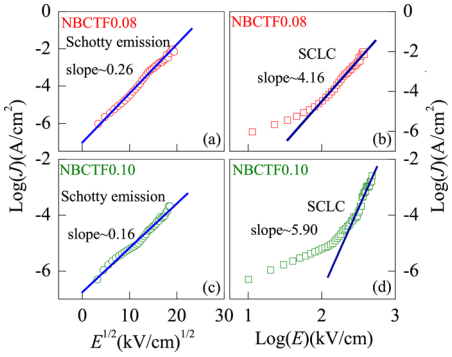

Figure 9. (a) $\log(J)-E^{1/2}$, (b) $\log(J)-\log(E)$ of the NBCTF0.08 film, (c) $\log(J)-E^{1/2}$, and (d) $\log(J)-\log(E)$ of the NBCTF0.10 film on the ($Pt/TiO_2/SiO_2/Si$) substrates measured at room temperature. Note that various fits of these data are shown to determine the leakage mechanism of the NBCTFx (x = 0.08 and 0.10) films and that the symbols and solid lines indicate the experimental data and fitting results, respectively.

was observed and the slopes are 0.26 and 0.16, respectively. So, the NBCTF0.10/Pt interface forms a Schottky barrier in the low electric field region, and the leakage current shows Schottky emission behavior. The conduction current from SCLC can be expressed as $J_{SCLC} = 9\mu\varepsilon_0\varepsilon_r E^2/8d$, where μ is the charge carrier mobility, ε_0 is the dielectric constant of free space, and ε_r and d are the relative dielectric constant and thickness of the films. Parts b and d of Figure 9 show the plots of $\log(J)$ versus $\log(E)$ for the NBCTF0.08 and NBCTF0.10 films; it can be seen that in the high electric field the plot of $\log(J)$ versus $\log(E)$ shows slopes that are close to 4.16 and 5.90 for the NBCTF0.08 and NBCTF0.10 films, respectively, which agrees well with the SCLC theory.[47] In general, the substitution of cerium can reduce the leakage current density and enhance the ferroelectric behavior by reducing oxygen vacancies, forming defect complexes, inducing lattice distortion, and so on. In the low-electric-field region, the Schottky emission is the dominating leakage process, while SCLC is considered as the dominating leakage mechanism of NBCTFx films in the high-electric-field region. Moreover, the NBCTFx films could have promising applications in solar cell and other ferroelectric optoelectronic fields because of the tunable band gap, compared to traditional perovskite ferroelectric materials.[49,50]

4. CONCLUSION

In summary, the NBCTFx nanocrystalline films were deposited on platinized silicon ($Pt/TiO_2/SiO_2/Si$) substrates by the sol–gel method employing a spin-coating process. XRD analysis results show that the films are polycrystalline and exhibit the pure perovskite-phase structure. Moreover, the grain sizes of the films decrease with increasing cerium composition, while the thicknesses of the films increase with increasing cerium composition. The dielectric functions of the NBCTFx films were uniquely extracted by fitting the measured ellipsometric data with the TL and four-phase-layered models. The fitted result indicates that the optical band gap of the films decreases with increasing cerium composition. The leakage current density of the films decreases with increasing cerium composition, and the optimal ferroelectric properties were obtained in the film with x = 0.10, which could be crucial for future applications for integration in devices.

AUTHOR INFORMATION

Corresponding Author

*Tel.: +86-21-54345150. Fax: +86-21-54345119. E-mail: zghu@ee.ecnu.edu.cn.

Notes

The authors declare no competing financial interest.

ACKNOWLEDGMENTS

S.Z. thanks Hao Zhang for $P-E$ experiments and Jian Liu for AFM measurements. This work was financially supported by the Major State Basic Research Development Program of China (Grants 2011CB922200 and 2013CB922300), Natural Science Foundation of China (Grants 11074076 and 61106122), Project of Science and Technology Commission of Shanghai Municipality (Grant 11520701300), Program for Professor of Special Appointment (Eastern Scholar) at Shanghai Institutions of Higher Learning, and Project from East China Normal University (Grant MXRZZ2012009).

REFERENCES

(1) Jaffe, B.; Cook, W. R.; Jaffe, H. *Piezoelectric Ceramics*; Academic: New York, 1971.
(2) Levassort, F.; Tran-Huu-Hue, P.; Ringaard, E.; Lethiecq, M. *J. Eur. Ceram. Soc.* **2001**, *21*, 1361–1365.
(3) Elkechai, O.; Marchetype, P.; Thomas, P.; Manier, M.; Mercurio, J.-P. *J. Mater. Chem.* **1997**, *7*, 91–97.
(4) Spreitzer, M.; Valant, M.; Suvorov, D. *J. Mater. Chem.* **2007**, *17*, 185–192.
(5) Takenaka, T.; Maruyama, K.; Sakata, K. *Jpn. J. Appl. Phys.* **1991**, *30*, 2236–2239.
(6) Hiruma, Y.; Watanabe, T.; Nagata, H.; Takenaka, T. *Jpn. J. Appl. Phys.* **2008**, *47*, 7659–7663.
(7) Rodel, J.; Jo, W.; Seifert, K. T. P.; Anton, E. M.; Granzow, T.; Damjanovic, D. *J. Am. Ceram. Soc.* **2009**, *92*, 1153–1177.
(8) Jin, D. Z.; Chen, X. M.; Xu, Z. C. *Mater. Lett.* **2004**, *58*, 1701–1705.
(9) Hiruma, Y.; Nagata, H.; Takenaka, T. *J. Appl. Phys.* **2009**, *105*, 084112/1–084112/8.
(10) Viehland, D. *J. Am. Ceram. Soc.* **2006**, *89*, 775–785.
(11) Davies, M.; Aksel, E.; Jones, J. L. *J. Am. Ceram. Soc.* **2011**, *94*, 1314–1316.
(12) Babu, J. B.; He, M.; Zhang, D. F.; Chen, X. L.; Dhanasekaran, R. *Appl. Phys. Lett.* **2007**, *90*, 102901/1–102901/3.
(13) Jiang, A. Q.; Li, G. H.; Zhang, L. D. *Ferroelectrics* **1998**, *215*, 103–111.
(14) Jiang, A. Q.; Zhang, L. D. *Phys. Rev. B* **1999**, *60*, 9204–9207.
(15) Kruzina, T. V.; Duda, V. M.; Suchanicz, J. *Mater. Sci. Eng. B* **2001**, *87*, 48–52.
(16) Zhao, M. L.; Wu, Q. Z.; Wang, C. L.; Zhang, J. L.; Gai, Z. G.; Wang, C. M. *J. Alloys Compd.* **2009**, *476*, 393–396.
(17) Roleder, K.; Franke, I.; Glazer, A. M.; Thomas, P. A.; Miga, S.; Suchanicz, J. *J. Phys.: Condens. Matter* **2002**, *14*, 5399–5406.
(18) Andriyevsky, B.; Suchanicz, J.; Cobet, C.; Patryn, A.; Esser, N.; Kosturek, B. *Phase Transitions* **2009**, *82*, 567–575.
(19) Yang, C. H.; Hu, G. D.; Wu, W. B.; Wu, H. T.; Yang, F. *Appl. Phys. Lett.* **2012**, *100*, 022909/1–022909/3.
(20) Bujakiewicz-Koroska, R.; Natanzon, Y. *Phase Transitions* **2008**, *81*, 1117–1124.
(21) Hosono, Y.; Harada, K.; Yamashita, Y. *Jpn. J. Appl. Phys.* **2001**, Part 1, *40*, 5722–5726.

(22) Xu, G.; Duan, Z.; Wang, X.; Yang, D. *J. Cryst. Growth* **2005**, Part 1, *275*, 113−119.
(23) Ge, W. *J. Alloys Compd.* **2008**, Part 1, *462*, 256−261.
(24) Yia, X.; Chen, H.; Cao, W.; Zhao, M.; Yang, D.; Ma, G.; Yang, C.; Han, J. *J. Cryst. Growth* **2005**, *281*, 364−369.
(25) Zhang, J. Z.; Shen, Y. D.; Li, Y. W.; Hu, Z. G.; Chu, J. H. *J. Phys. Chem. C* **2010**, *114*, 15157−15164.
(26) Azzam, R. M. A.; Bashara, N. M. *Ellipsometry and Polarized Light*; North-Holland: Amsterdam, The Netherlands, 1977.
(27) Wang, Y.; Jiang, Q. H.; He, H. C.; Nan, C. W. *Appl. Phys. Lett.* **2006**, *88*, 142503/1−142503/3.
(28) Mullins, D. R.; Overbury, S. H.; Huntley, D. R. *Surf. Sci.* **1998**, *409*, 307−319.
(29) Gavarini, S.; Guittet, M. J.; Trocellier, P.; Gautier-Soyer, M.; Carrot, F.; Matzen, G. *J. Nucl. Mater.* **2003**, *322*, 111−118.
(30) Mekki, A. *J. Electron Spectrosc. Relat. Phenom.* **2005**, *142*, 75−81.
(31) Bêche, E.; Charvin, P.; Perarnau, D.; Abanades, S.; Flamant, G. *Surf. Interface Anal.* **2008**, *40*, 264−267.
(32) Kolmakov, A.; Potluri, S.; Barinov, A.; Mentes, T. O.; Gregoratti, L.; Nino, M. A.; Locatelli, A.; Kiskinova, M. *ACS Nano* **2008**, *2*, 1993−2000.
(33) Shannon, R. D. *Acta Crystallogr.* **1976**, *A32*, 751−767.
(34) Anooz, S. B.; Schwarzkopf, J.; Dirsyte, R.; Ehrstein, E.; Petrik, P.; Kwasniewski, A.; Wagner, G.; Fornari, R. *Thin Solid Films* **2011**, *519*, 3782−3788.
(35) Cho, Y. J.; Nguyen, N. V.; Richter, C. A.; Ehrstein, J. R.; Lee, B. H.; Lee, J. C. *Appl. Phys. Lett.* **2002**, *80*, 1249−1251.
(36) Jellison, G. E., Jr.; Modine, F. A. *Appl. Phys. Lett.* **1996**, *69*, 371−373.
(37) Hu, Z. G.; Ma, J. H.; Huang, Z. M.; Wu, Y. N.; Wang, G. S.; Chu, J. H. *Appl. Phys. Lett.* **2003**, *83*, 3686−3688.
(38) Kvietkova, J.; Daniel, B.; Hetterich, M.; Schubert, M.; Spemann, D.; Litvinov, D.; Gerthsen, D. *Phys. Rev. B* **2004**, *70*, 045316/1−045316/7.
(39) Hu, Z. G.; Hess, P. *Appl. Phys. Lett.* **2006**, *89*, 081906/1−081906/3.
(40) Zeng, M.; Or, S. W.; Chan, H. L. W. *J. Appl. Phys.* **2010**, *107*, 043513/1−043513/5.
(41) Yu, T.; Kwok, K. W.; Chan, H. L. W. *Thin Solid Films* **2007**, *515*, 3563−3566.
(42) Moulson, A. J.; Herbert, J. M. *Electroceramics: Materials, Properties, Applications*, 2nd ed.; John Wiley & Sons: New York, 2003; pp 52−60 and 358−360.
(43) Scott, J. F.; Melnick, B. M.; Araujo, C. A.; McMillan, L. D.; Zuleeg, R. *Integr. Ferroelectr.* **1992**, *1*, 323−331.
(44) Zafar, S.; Jones, R. E.; Jiang, B.; White, B.; Kaushik, V.; Gillespie, S. *Appl. Phys. Lett.* **1991**, *70*, 382−384.
(45) Watanabe, K.; Hartmann, A. J.; Lamb, R. N.; Scott, J. F. *J. Appl. Phys.* **1998**, *84*, 2170−2175.
(46) Wang, Y.; Tseng, T. Y. *J. Appl. Phys.* **1997**, *81*, 6762−6770.
(47) Scott, J. F. *Ferroelectric Memories*; Springer: Berlin, 2000.
(48) Sze, S. M. *Physics of Semiconductor Device*, 2nd ed.; Wiley: New York, 1981; pp 438−453.
(49) Huang, H. T. *Nat. Photonics* **2010**, *4*, 134−135.
(50) Yang, S. Y.; Seidel, J.; Byrnes, S. J.; Shafer, P.; Yang, C.-H.; Rossell, M. D.; Yu, P.; Chu, Y.-H.; Scott, J. F.; Ager, J. W., III; Martin, L. W.; Ramesh, R. *Nat. Nanotechnol.* **2009**, *5*, 143−147.